Three-Dimensional Design Optimization Of An Anode-Supported SOFC Using FEM

Andersson, Martin; Yuan, Jinliang; Sundén, Bengt

Published in:
ECS Transactions

DOI:
10.1149/05701.2485ecst

2013

Three-Dimensional Design Optimization of an Anode-Supported SOFC using FEM

M. Andersson [a], J. Yuan [a] and B.Sundén [a]

[a] Department of Energy Sciences, Lund University, Box 118, 22100 Lund, Sweden

Solid oxide fuel cells (SOFCs) are promising as energy producing devices, which at this stage of development will require extensive analysis and benefit from numerical modeling. A 3D model is developed based on the FEM for a single cell planar SOFC design optimization. Ion, electron, heat, gas-phase species and momentum transport equations are implemented and coupled to the kinetics of electrochemical reactions. High current density spots are identified, where the electron transport distance is short and the oxygen concentration is high. The relatively thin cathode results in a significant oxygen mole fraction gradient in the direction normal to the main flow direction. The electron transport especially within the cathode is found to be limiting for the electrochemical reactions at positions far from the channel walls (interconnect ribs). It is concluded that an increased pore size in the cathode support layer increases the current density more than an increased pore size in the anode support layer.

Introduction

Ever increasing energy consumption, higher prices for fossil fuels and rising public awareness for environmental protection have motivated studies looking for renewable/alternative energy sources. Among different types of small-scale power generation systems, fuel cells (FCs) have received more attention since they provide both power and heat. FCs are static energy conversion devises, which partially convert the chemical energy of fuels directly into electrical energy with water as byproduct if pure hydrogen is supplied. The basic principle of the fuel cell was discovered by the Swiss scientist Christian Friedrich Schönbein in the year 1838. Sir William Grove developed the first fuel cell in 1839 (1-2).

Solid oxide fuel cells (SOFCs) have the possibility to improve energy efficiency. The high operating temperature (500 - 1000 °C) enables the SOFC to operate with existing fossil fuels to give a high electrical efficiency. Disadvantages with the high operating temperature include potential thermal fatigue failure of the cell functional materials and sealing. SOFCs are complex electrochemical devices that contain three basic components: a porous cathode, an electrolyte and a porous anode. The porous electrodes are of critical importance for the SOFC performance. The cathode is typically an oxide that catalyses oxygen reduction reaction (eqn [1]). The anode catalyses the oxidation of fuel (eqn [2]) (2-3).

$$\frac{1}{2}O_2 + 2e^- \Leftrightarrow O^{2-} \qquad [1]$$

$$H_2 + O^{2-} \Leftrightarrow H_2O + 2e^- \quad [2]$$

The porous electrodes are normally fabricated following this procedure: mixing of electrode material with organic porous former, dry-pressing of the mixture. The organic porous former is removed during the sintering process, and simultaneously comes the fine ceramic particles come into contact with each other. The smaller particles may coalesce with larger particles, giving particle agglomeration. It should be noted that since the porosity of electrodes fabricated using such a method is distributed randomly, it may change from one fabrication process to another (2).

The aim of this paper is to investigate the impact from different pore and particle sizes in the electrode active and support layers, respectively, on the current density and the polarizations distribution, for an anode-supported planar SOFC. The methodology applied in this study is the FEM.

Modeling Equations and Method

A 3D model for a planar anode-supported SOFC is developed and implemented in the commercial software COMSOL Multiphysics (version 4.3.1.161). Equations for electron, ion, gas-phase species, momentum and heat transport to be solved are coupled to kinetics describing the electrochemical reactions. The geometry is defined in reference (4) and the applied cell parameters are outlined in reference (5).

Due to internal resistance and polarizations (η) the actual voltage (E) becomes less than the open-circuit voltage. The actual voltage can be expressed as (6):

$$E = E^{OCV} - \eta_{act} - \eta_{ohm} - \eta_{conc} \quad [3]$$

The activation polarizations are defined as:

$$\eta_{act,a} = \phi_s - \phi_l - E_{eq,a} \quad [4]$$

$$\eta_{act,c} = \phi_s - \phi_l - E_{eq,c} \quad [5]$$

where ϕ is the potential, E_{eq} the equilibrium voltage. The index a stands for the anode, c for the cathode, s for the electrode (metal) material and l for the electrolyte (YSZ) material. The concentration polarizations are specified in (8). The electromotive force (reversible open-circuit voltage, E^{OCV}) is determined by the difference in the thermodynamic potentials of the electrode reactions, as described in (5)-(8). The current density can be obtained through the reduced Butler-Volmer equation (7):

$$i = 2 \cdot AV \cdot i_0 \cdot \sinh\left(\frac{n_e \cdot \mathrm{F} \cdot \eta_{act,e}}{2 \cdot \mathrm{R} \cdot T}\right) \quad [6]$$

$$i_0 = \frac{\mathrm{R}\cdot T}{n_e \cdot \mathrm{F}} \cdot k_e'' \cdot \exp\left(\frac{-E}{\mathrm{R}\cdot T}\right) \qquad [7]$$

where i is the current density, F Faraday's constant, k_e'' the pre-exponential factor (which is $6.54\cdot10^{11}\ \Omega^{-1}\mathrm{m}^{-2}$ for the anode and $2.35\cdot10^{11}\ \Omega^{-1}\mathrm{m}^{-2}$ for the cathode (5)), i_0 the exchange current density, n_e the number of electrons transferred per reaction, $\eta_{act,e}$ the electrode activation polarization, R the ideal gas constant, AV_e the electrochemical active area to volume ratio and $E_{a,e}$ is the activation energy (137 kJ/mol for the cathode and 140 kJ/mol for the anode (6)). The potential difference between the anode and the cathode current collectors corresponds to the total cell operating voltage. The governing equations for the ion and electron transport are implemented according to eqns [8]-[9].

$$i_l = \nabla \bullet \left(-\sigma_l \nabla \phi_l\right) \qquad [8]$$

$$i_s = \nabla \bullet \left(-\sigma_s \nabla \phi_s\right) \qquad [9]$$

where ϕ is the potential and σ is the ion/electron conductivity. The electronic conductivities in the anode ($\sigma_{s,a}$) and the cathode ($\sigma_{s,c}$), and ionic conductivity in the YSZ ($\sigma_{l,el}$) are calculated as described in our previous work (8). The actual length that ions and electrons are transported in the electrodes increases because of the real/functional material compositions and their micro structures. This is accounted for by using the structure-dependent tortuosities and volume fractions (8).

The gases flow inside the fuel cell components, such as in the fuel and air channels, and in the porous electrodes. Equation [10] is introduced and solved for the momentum transport in the fuel and air channels, and in the porous materials, simultaneously (9-10).

$$\left(\frac{\mu}{\kappa} + \rho \cdot \nabla \bullet \vec{\mathrm{u}}\right) \cdot \vec{\mathrm{u}} - \nabla\left[-p + \frac{1}{\varepsilon}\left\{\Psi - \left(\frac{-2}{3}\cdot\mu\right)(\nabla \bullet \vec{\mathrm{u}})\right\}\right] = \mathbf{F} \qquad [10]$$

Here **F** is the volume force vector, p the pressure, κ the permeability of the porous medium ($1.76\ \cdot10^{-11}\ \mathrm{m}^2$), $\vec{\mathrm{u}}$ the velocity vector, Ψ the viscous stress tensor. The viscosity (μ) and density (ρ) for the participating gas mixtures are dependent on local temperature and mole fractions, as described in (5).

In the porous material, there are two kinds of gas-phase species diffusion mechanisms; Knudsen (collisions between the gas molecules and the pore walls) and molecular (collisions between two different gas molecules) diffusions. Equation [11] is used to describe the gas-phase species transport phenomena for each component inside the cell (10) and solved for the air- and fuel channels and the electrodes.

$$\nabla\left(-\rho \cdot w_i \sum^{n} D_{\mathrm{eff},ij} \cdot \nabla x_j + \left(x_j - w_j\right)\frac{\nabla p}{p} \bullet \vec{\mathrm{u}} - D_i^T \cdot \frac{\nabla T}{T}\right) + \rho \cdot \vec{\mathrm{u}} \cdot \nabla w_j = S_i \qquad [11]$$

where T is the temperature, x the mole fraction, w the mass fraction, D_i^T the thermal diffusion coefficient and S_i the source term due to electrochemical reactions. A local

temperature equilibrium (LTE) approach is applied, where the overall governing equation for heat transport (eqn [12]) reduces to pure heat conduction in the electrolyte layer and in the interconnector.

$$\rho_g \cdot c_{p,g} \cdot \vec{u} \cdot \nabla T = \nabla \bullet \left(k_{eff} \nabla T \right) + Q_h \qquad [12]$$

Here Q_h is the heat generation/consumption, k_{eff} the effective thermal conductivity and c_p the gas-phase specific heat. The heat flux Q_h is based on heat generation by the electrochemical reactions and on the losses through the activation, the ohmic and the concentration polarizations (11).

$$Q_h = i \cdot \left(\frac{T \cdot \Delta S_r}{n_e \cdot F} + \eta_{act} + \eta_{conc} \right) + \sum \frac{i^2}{\sigma} \qquad [13]$$

where ΔS_r is entropy change of the reaction.

The gas inlet velocities are defined as a laminar flow profile, and the average values are based on the oxygen- and hydrogen utilization, i.e., 9 % and 76 % are specified, respectively, for the standard case in this study. At the outlets the pressure (1 atm) is fixed. The fuel inlet fractions are defined as 10 % (mole) water and 90 % (mole) hydrogen. The air consists of nitrogen and oxygen. The channel outlets are defined as convective flux. The inlet gas temperature is defined by the operating temperature (1000 K) and the outlet is defined as a convective flux. The electric potential at the anode current collector is set to zero and the potential at the cathode current collector is set as the cell operating voltage (0.7 V). All other boundaries and interfaces are electrically insulated.

The simulation is conducted for four cases:

- Standard case without modification of the electrode support layer pore size
- The anode support layer pore size is increased with a factor of 5.
- The cathode support layer pore size is increased with a factor of 5.
- The anode and cathode support layers pore size is increased 5 times.

Results and Discussion

The current density distribution at the cathode/electrolyte interface for the standard case (without any electrode support layer modification) is presented in Fig. 1. Note that the scales on the axes are made dimensionless according to eqns. (14)-(15). The current density rises along the main flow direction as the temperature increases. This rise is limited due to the electrochemical reaction related product generation and reactant consumption along the main flow direction. In the direction normal to the main flow direction (z*-direction in Fig. 1) the current density is highest close to the channel/interconnect interfaces, i.e., where the electron transport distance is short and the concentration of oxygen is high.

$$x^* = x / L \qquad [14]$$

$$z^* = z/W \quad [15]$$

Here, W is the width of the fuel/air channel (=2 mm) and the corresponding ribs (=0.5+0.5 mm), as well as L is the cell length along the main flow direction (=100 mm).

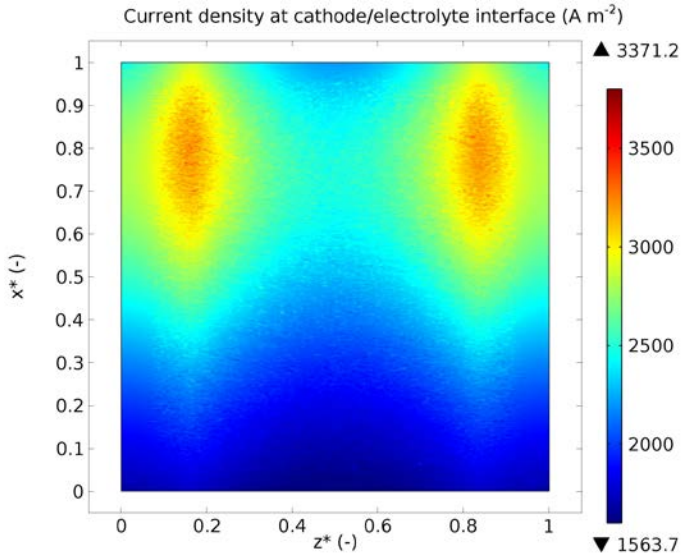

Figure 1. Without support layer pore size modification. (0) at the x*-axis corresponds to the inlet and (1) to the outlet. (0.167) and (0.833) at the z*-axis corresponds to the interconnect/channel interfaces.

Figure 2 presents the current density at the cathode/electrolyte interface as the pore size (and indirectly also the particle size) within the anode support layer is increased with a factor of 5 compared to the pore size within the active layer closest to the electrolyte. The maximum and the average current densities are increased by only around 0.3 %, compared to the case without modification of the support layer pore size (in Fig. 1).

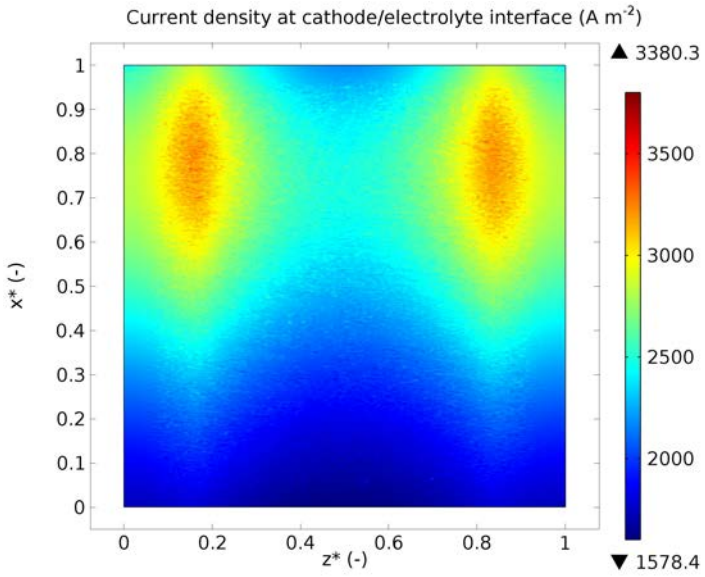

Figure 2. Anode support layer pore size modification effect.

The current density as the pore size within the cathode support layer is increased by a factor of 5 is shown in Fig. 3. It is clear that an increased support layer pore size within the cathode gives significantly more influence on the current density, compared to the anode case (Fig. 2). The maximum current density increases by around 2.5 %, compared to the case with no modification (in Fig. 1). The reason for the bigger impact from the cathode side modification is the relatively thin cathode giving a large transport resistance in the cathode under the interconnect ribs.

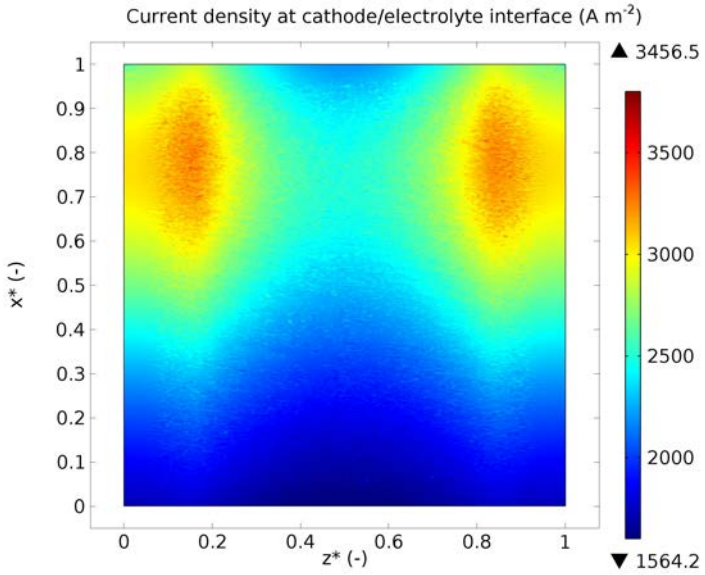

Figure 3. Cathode support layer pore size modification effect.

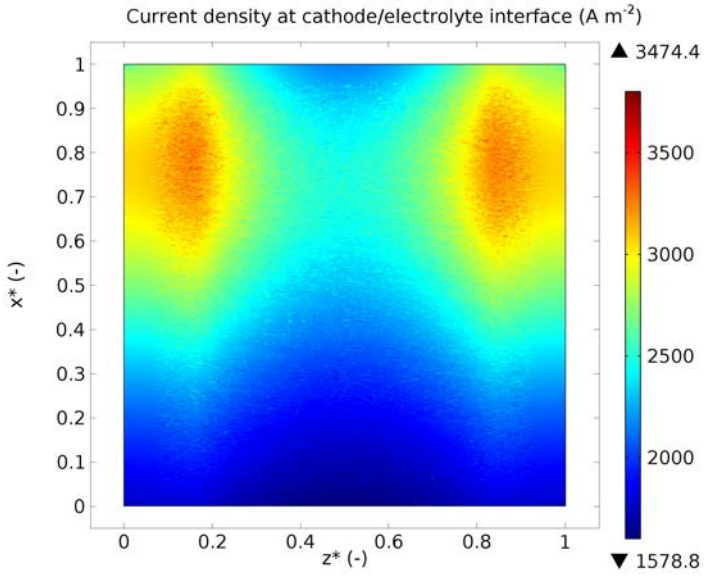

Figure 4. Anode- and cathode support layer pore size modification effect.

Figure 4 presents the current density distribution for the case where the pore size of both the anode and the cathode support layers are increased by a factor of 5 compared to respective active layers. It is seen that the maximum current density increases by around 3 %, compared to the case without support layer pore size modification. The slightly bigger increase compared to the sum of the anode and cathode modification (2.8 %) can be explained by the strong coupling between the temperature and the current density, i.e., an increased current density at the inlet increases the local temperature (not shown in this paper), which increases the current density along the main flow direction.

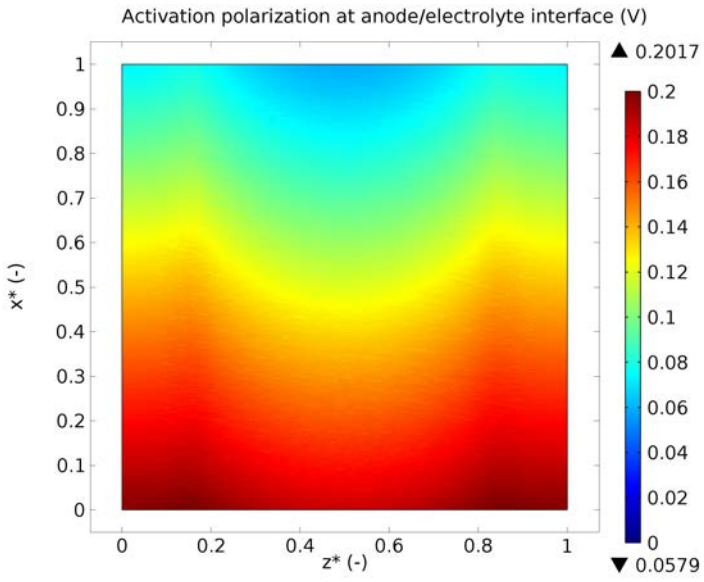

Figure 5. Anode- and cathode support layer pore size modification effect.

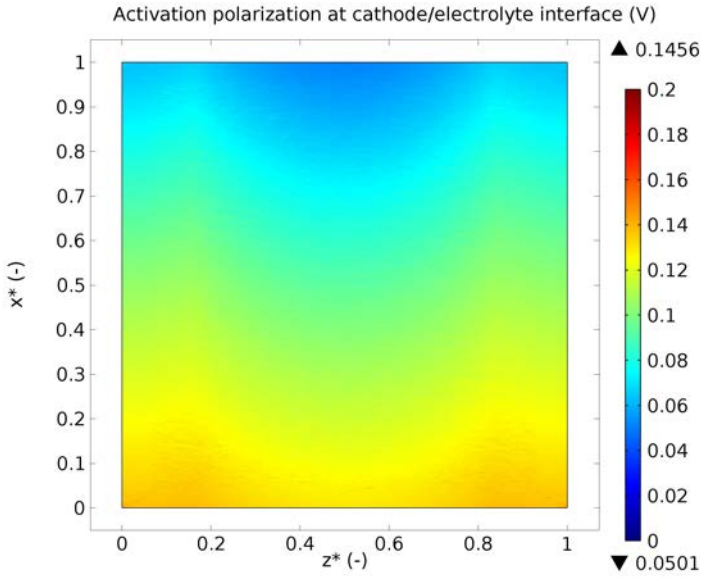

Figure 6. Anode- and cathode support layer pore size modification effect.

The activation polarization at the anode/electrolyte interface is presented in Fig. 5 for the case with an increased pore size within both the anode and cathode support layers and the one at the cathode/electrolyte interface in Fig. 6. Notice that the color scale is identical for Figs 5 and 6. It is found that the activation polarizations are highest at the inlet, corresponding to a high OCV. The activation polarization gradient in the direction normal to the main flow direction (z*-direction) is coupled to the OCV gradient in the same direction, but depends also on the concentration and ohmic polarizations. The model presented here predicts a slightly higher activation polarization within the anode (Fig. 5), compared to the one in the cathode (Fig. 6). It is seen that the difference between direction. Note that the current density and the activation polarizations are highest at the electrode/electrolyte interface and decreases rapidly within the electrodes as the distance to the interface increases (note that this direction is not shown in the presented figures). On the other hand, the ohmic polarization increases at positions far from the interface.

The concentration polarization, for the case with an increased pore size within both the anode and cathode support layers, is presented in Fig. 7 for the anode/electrolyte interface and in Fig. 8 for the cathode/electrolyte interface. Note that the color scale in Fig. 7 and in Fig. 8 is the same. It is shown that the concentration polarization is noteworthy for positions under the interconnect ribs and also that the anode one is much smaller than the cathode one. The highest values are found close to the outlet, where the gradients of hydrogen and oxygen in the direction normal to the main flow direction are highest. For the anode an effect at the inlet can also be seen due to the relatively thick anode. It is found that at positions under the rib and close to outlet the concentration polarization corresponds to around 10 % of the total polarizations. At the positions under the fuel and air channels the concentration polarization is less than 1 % of the total polarizations.

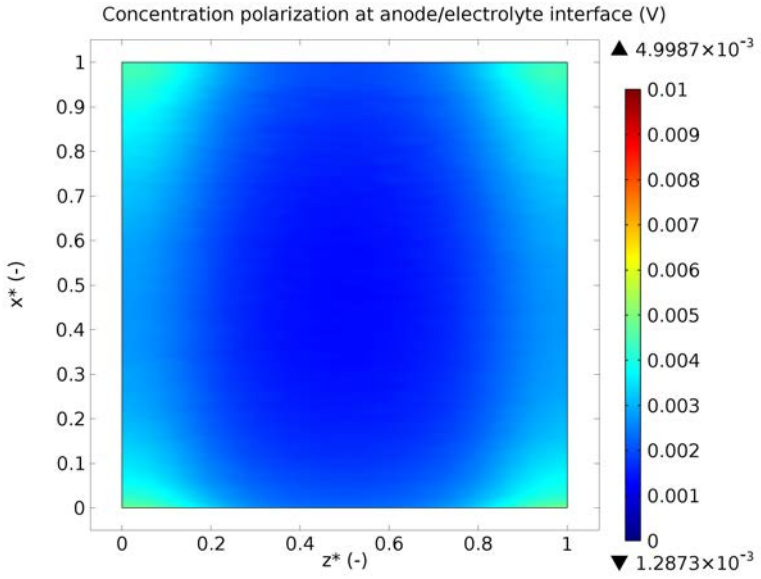

Figure 7. Anode- and cathode support layer pore size modification effect.

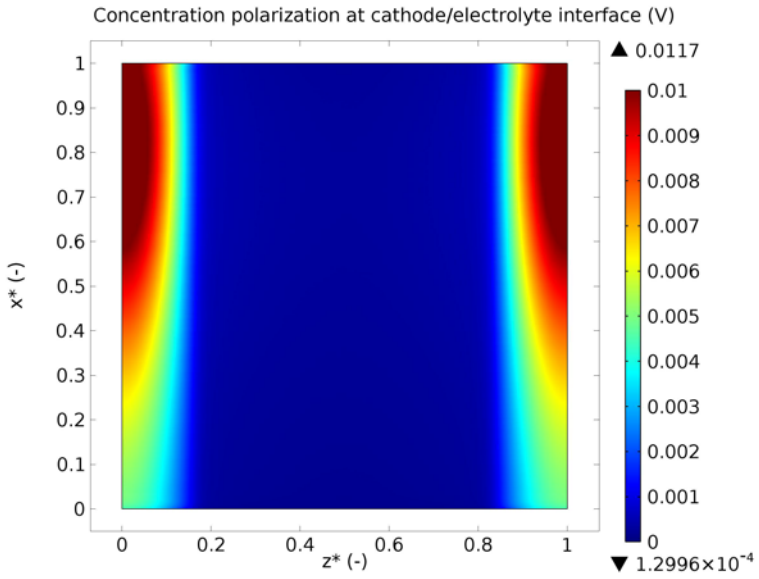

Figure 8. Anode- and cathode support layer pore size modification effect.

Due to the similarity for the different polarization distributions between the different cases only some minimum and maximum values are presented in Table I. The anode activation polarization has its highest maximum for the case with modification of both the anode and cathode support layers and its lowest maximum for the case without pore size modification, because a decreased concentration polarization, due to decreased gas-phase mass transport resistance from the increased pore size in the support layers, increases the voltage available for activation polarization, i.e., increasing the current density. It is clear that the impact from the cathode dominates over the anode one. The minimum activation polarization decreases from an increased outlet temperature (which decreases the OCV) as the support layer pore size is increased. For the activation polarization on the cathode side the same trends as on the anode side can be seen. The maximum concentration polarization is more than doubled in the cathode compared to the anode. An increased support layer pore size (with 5 times) reduces the maximum concentration polarization within both the anode and cathode with more then 50 %. Interesting is that the cathode maximum concentration polarization increases as the anode support layer pore size is increased, due to an increased current density and more oxygen consumed, and consequently the anode maximum concentration polarization is slightly increased as the cathode support layer pore size is increased.

TABLE I. Extreme polarizations (V)

Modification:	**Without**	**An. + Cat.**	**Anode**	**Cathode**
Anode activation polarization max	0.1992	0.2017	0.1995	0.2014
Anode activation polarization min	0.0602	0.0579	0.0588	0.0596
Cathode activation polarization max	0.1429	0.1456	0.1444	0.1441
Cathode activation polarization min	0.0523	0.0501	0.0517	0.0509
Anode concentration polarization max	0.0098	0.0045	0.0049	0.0106
Cathode concentration polarization max	0.0246	0.0117	0.0249	0.0115

Conclusions

A FEM approach is developed to investigate various chemical and physical phenomena inside a single cell of a planar anode-supported SOFC. The coupled equations for momentum, gas-phase species, electron, ion and heat transport are solved with kinetic expressions for electrochemical reactions in the electrodes. The current density increases along the main flow direction, due to the increased temperature from the electrochemical reactions. This increase is limited due to the consumption of electrochemical reactants within the cell. It is found that a large current density gradient appears in the active electrode regions corresponding to the positions under the ribs between the channels, due to the increased resistance for the electron and the gas-phase oxygen transport. It is noted that, for the case where both the anode and cathode support layer pore size is increased (five times), at the positions under the rib and close to outlet, the concentration polarization corresponds to around 10 % of the total polarizations, compared to around 20 % for the standard case. At the positions under the fuel and air channels the part corresponding to concentration polarization is less than 1 % of the total polarization. As the anode and cathode support layer pore size (and indirectly also the particle size) is increased five times, the maximum current density increases 3 %, compared to an increase of 0.3 % if only the anode support layer pore size is increased and of 2.5 % if only the cathode support layer pore size is increased.

Acknowledgments

The financial support from the Swedish Research Council (VR-621-2010-4581) and the European Research Council (ERC-226238-MMFCs) is gratefully acknowledged.

References

1. S.A. Hajimolana M.A. Hussain, W.M.A. Wan Daud, M. Soroush, A. Shamiri, *Renewable and Sustainable Energy Reviews*, **15**, 1893-1917 (2011).
2. J. Shi, X. Xue, *Electrochmica Acta*, **56**, 8718-8726 (2011).
3. A.J. Jacobsson, *Chem. Mater.*, **22**, 660-674 (2010).
4 . M. Andersson, H. Paradis, J. Yuan, B. Sundén, ASME-ESFuelCell2013-18005 (2013).
5. M. Andersson, J. Yuan, B. Sundén, *Int. J. Heat Mass Transfer* **55**, 773-788 (2012).
6. Y. Patcharavorachot, A. Arpornwichanop, A. Chuachuebsuk, *J. Power Sources*, **177**, 254-261. (2008).
7. A.S. Joshi, A.A. Peracchio, K.N. Grew, W.K.S. Chiu, *J. Phys. D: Appl. Phys.*, **40** 7593-7600 (2007).
8. M. Andersson, J. Yuan, B. Sundén, *J. Power Sources*, **232,** 42-54 (2013).
9. M. le Bars, M.G. Worster, *J. Fluid Mech.*, **550,** 149-173 (2006).
10. COMSOL Multiphysics Version 4.3 User Guide, Stockholm, Sweden (2012).
11. M. Andersson, H. Paradis, J. Yuan, B. Sundén, *J. Fuel Cell Science and Technology*, **8,** 031013 (2011).